

Magnetic field induced partially polarized chiral spin liquid in a transition metal dichalcogenide moiré system

Yixuan Huang,^{1,2} D. N. Sheng,³ and Jian-Xin Zhu^{1,2,*}

¹*Theoretical Division, Los Alamos National Laboratory, Los Alamos, New Mexico 87545, USA*

²*Center for Integrated Nanotechnologies, Los Alamos National Laboratory, Los Alamos, New Mexico 87545, USA*

³*Department of Physics and Astronomy, California State University, Northridge, California 91330, USA*

(Dated: April 9, 2024)

As one of the most intriguing states of matter, the chiral spin liquid (CSL) has attracted much scientific interest while its existence and mechanism in crystalline strongly correlated systems remain hotly debated. On the other hand, strong correlation driven emergent phenomena can be realized in twisted transition metal dichalcogenide bilayers with a tremendously tunable large length scale providing a new platform for the emergence of CSLs. We focus on a strongly correlated model relevant to heterobilayer $\text{WSe}_2/\text{MoSe}_2$ and investigate the Mott insulating phase at half filling under an out-of-plane magnetic field. Considering both its orbital and spin Zeeman effects we identify three conventionally ordered phases including a 120° Néel phase, a stripe phase, and an up-up-down phase. For intermediate fields an emergent quantum spin liquid phase is identified with partial spin polarization. We further characterize its topological nature as the $\nu = 1/2$ Laughlin CSL through the topological entanglement spectrum and quantized spin pumping under spin flux insertion. In addition, we map out the quantum phase diagram for different twisted angles in an experimentally accessible parameter regime.

I. INTRODUCTION

Quantum spin liquids [1–4] (QSLs) are exotic states of matter that feature non-trivial topology [5–7] and fractionalized excitations [8]. The novel properties of QSLs have attracted numerous studies for several decades which provide potential ways to realize unconventional superconductivity through doping QSLs [9–12], and enable topological quantum computation [13, 14]. Furthermore, it has been proposed that the behaviors of many more exotic correlated electronic systems such as the holon Wigner crystal and strange metal can be understood from the perspective of doping QSLs [15–17]. However, candidate materials of QSLs are very rare partially because of the lack of definite evidence to detect QSLs in experiments.

As a promising example, the chiral spin liquid (CSL) carries a quantized chiral edge current that realizes the bosonic version of the fractional quantum Hall effect (FQHE). As a result, CSL may be identified through the quantized thermal Hall conductivity [18–20]. Upon doping, CSL can lead to topological superconductivity [21] that supports Majorana edge excitations, responsible for edge zero-biased peaks in experiments [22]. Recently, such novel states have been found numerically on realistic triangular lattice models such as the Hubbard model [23, 24], and the extended Heisenberg model [25] supplemented by three-spin chiral interactions [26–29] or four-spin ring exchanges [30]. However, higher-order terms that involve more spins are generally small in perturbation theory and cannot be tuned without considering the interplay among different effective spin inter-

actions. Furthermore, the range of relative strength between nearest neighbor and further neighbor interactions is not fully accessible for most candidate materials that show spin-liquid like behaviors [31–38]. Thus, the numerical identification for CSLs based on real material parameters remains inconclusive.

Recently, it has been proposed that twisted transition metal dichalcogenide (TMD) bilayers can simulate Hubbard model physics with tunable interacting strengths by different twisted angles [39–43]. In particular, the $\text{WSe}_2/\text{MoSe}_2$ heterobilayer has a single flat band that can be isolated with hole doping, leading to an effective Hubbard model with competing interactions on triangular moiré superlattices [39]. Even more appealingly, owing to the significantly larger unit cell, an experimentally accessible magnetic field can generate large magnetic flux per unit cell to induce strong effective chiral interactions that are impossible in conventional solid state crystalline systems [27, 44–47]. However, considering the Zeeman term the system energy can be reduced by flipping the spins into a partially polarized state, which makes the non-magnetic CSL, a robust quantum Hall state [28], an excited state. Thus, whether the ground state can be a CSL with a quantized Chern number in a finite magnetization state remains an open question.

Motivated by the possible field induced chiral spin liquids in TMD moiré systems, we study the emergent phases of the half-filled Hubbard model in the presence of an applied out-of-plane magnetic field based on the parameters of the $\text{WSe}_2/\text{MoSe}_2$ moiré bilayer. Through large-scale density matrix renormalization group (DMRG) simulations [48, 49] and considering both orbital and spin Zeeman effects of the magnetic field, we identify a CSL with partial spin polarization [50] at intermediate magnetic fields. In particular, the topological nature of the CSL is identified as the $\nu =$

* jxzhu@lanl.gov

1/2 FQHE through spin flux insertion simulations and a topological entanglement spectrum. We also show that the Chern number remains almost quantized in the presence of weak disorders. Applicable to the $\text{WSe}_2/\text{MoSe}_2$ heterobilayer setting, we map out the global quantum phase diagram using experimentally tunable parameters which are twisted angles and magnetic fields. Besides CSL, we identify stripe and up-up-down (UUD) phases with finite magnetization at larger magnetic fields, as well as a 120° Néel phase at smaller fields. Our results show that the interplay between orbital and spin effects of the applied magnetic field gives rise to a partially polarized-CSL (PP-CSL), which is stabilized in an experimentally accessible parameter regime. The robust Chern number in finite magnetization and disorder is relevant to the plateau of quantized thermal Hall conductance [18, 20] and can be tested in TMD moiré systems.

The rest of the paper is organized as follows: In Sec. II, we introduce the effective spin model and numerical methods used in this work. In Sec. III, we present our main findings in the phase diagram including various magnetic phases and an emergent PP-CSL phase. In Sec. IV, we further show numerical evidence of the magnetic phases. In Sec. V, we elucidate the nature of the PP-CSL from the entanglement spectrum and the quantized spin pumping via spin flux insertion, which is robust even under a weak disorder. We also discuss the stripelike spin polarization in the CSL phase. In Sec. VI, we give a summary and discussion.

II. MODELS AND METHODS

Considering a heterobilayer with similar lattice constants like $\text{WSe}_2/\text{MoSe}_2$, the moiré pattern can be formed with a large moiré lattice constant a_m and a small twisted angle θ_m [40]. Following Ref. [39], the low-energy bands can be approximated by a single-band Hubbard model with only spin degeneracy, where the Hamiltonian is given as

$$H_H = \sum_{\{ij\},\sigma} (-t_{ij} e^{i\frac{2\pi e}{h} \mathbf{A} \cdot (\mathbf{r}_i - \mathbf{r}_j)} c_{i\sigma}^\dagger c_{j\sigma} + \text{h.c.}) \quad (1)$$

$$+ U \sum_i n_{i\uparrow} n_{i\downarrow} + h_z \sum_i (c_{i\uparrow}^\dagger c_{i\uparrow} - c_{i\downarrow}^\dagger c_{i\downarrow}),$$

where we consider the nearest-neighbor (NN) hopping t_1 , next-NN hopping t_2 , and the on-site Coulomb repulsion U . An applied out-of-plane magnetic field affects both the orbital as the vector potential $\nabla \times \mathbf{A} = \mathbf{B}$, and the spin as the Zeeman effect $h_z = \frac{1}{2} \mu_B g_s B$, where μ_B is the Bohr magneton and the spin g -factor $g_s \approx 2$.

At half filling of the moiré bands U is much larger than t_1 [39], thus the charges are localized in the Mott insulating state. The effective spin model can be derived from the perturbation expansion of t/U [51] with effective three-spin chiral interactions [45] from the magnetic flux.

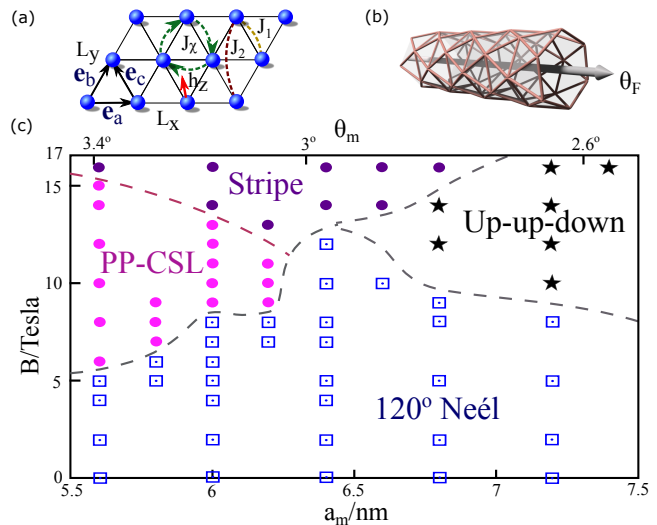


FIG. 1. (a) Illustration of a triangular lattice with various effective spin interactions. (b) Illustration of flux insertion simulations through the cylinder. (c) Global quantum phase diagram of the moiré lattice constant a_m and the corresponding twisted angle θ_m vs the magnetic field B , obtained on $L_y = 6$ cylinders. We identify 120° Néel, UUD, partially polarized-CSL, and stripe phases. The details of spin values in real space for these phases are presented in SM [52].

The overall spin Hamiltonian becomes

$$H_S = J_1 \sum_{\langle ij \rangle} \mathbf{S}_i \cdot \mathbf{S}_j + J_2 \sum_{\langle\langle ij \rangle\rangle} \mathbf{S}_i \cdot \mathbf{S}_j$$

$$+ J_\chi \sum_{\{ijk\} \in \Delta/\nabla} \mathbf{S}_i \cdot (\mathbf{S}_j \times \mathbf{S}_k) + 2h_z \sum_i S_i^z. \quad (2)$$

Here $\langle ij \rangle$ and $\langle\langle ij \rangle\rangle$ refer to the NN and next-NN site pair, and $\{ijk\}$ in the summation refers to three neighboring sites of every unit triangle taken clockwise [Fig. 1 (a)]. The strengths in the effective spin couplings are $J_1 = 4t_1^2/U - 28t_1^4/U^3$, $J_2 = 4t_2^2/U + 4t_1^4/U^3$, and $J_\chi = 24t_1^3 \sin(e\Phi_B/\hbar)/U^2$, where $\Phi_B = 2\pi B \frac{\sqrt{3}}{4} a_m^2$ is the magnetic flux through each unit triangle with a_m being the lattice constant of the triangular moiré superlattice. Other chiral interactions originating from ring geometries beyond the minimal triangular can also slightly enhance the chiral effect, which are not included here for simplicity. As a remarkable observation, the enlarged length scale of a_m significantly amplifies the orbital effect of magnetic fields, which in turn enhances chiral spin interactions over that in regular solid state crystalline systems by orders of magnitude.

We adopt the moiré lattice constant a_m dependence of t_1 , t_2 and U from Ref. [39]. As such, the coupling parameters in Eq. (2) are ultimately determined by a_m and B ; see more details in the Supplemental Material (SM) [52]. We explore different phases by tuning a_m between 5.5 and 7.5 nm, and B from 0 up to 17 T, as explained later.

The numerical results are obtained by both finite and

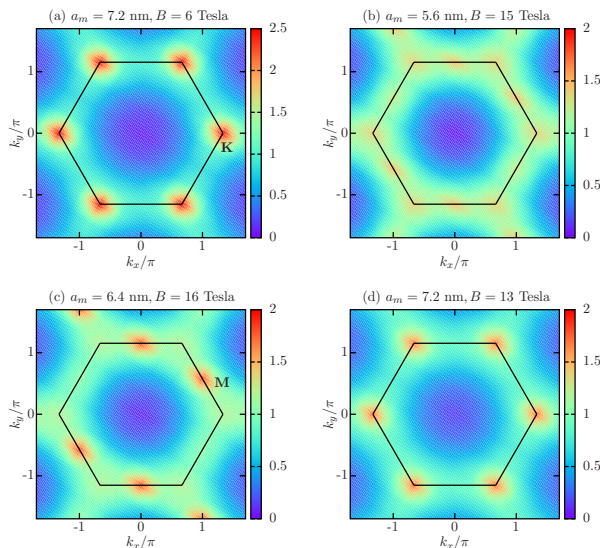


FIG. 2. Spin structure factor for (a) 120° Néel phase, (b) partially polarized-CSL, (c) stripe phase, (d) UUD phase, obtained on $L_y = 6$ systems.

infinite DMRG methods [53] with $U(1)$ spin symmetry [54, 55]. In flux insertion simulations, a flux θ_F is adiabatically inserted through the cylinder, as illustrated in Fig. 1 (b). The system has an open boundary in the e_a or x direction and periodic boundary conditions in the e_b or y direction [Fig. 1 (a)], with the number of sites denoted as L_x and L_y , respectively. The total number of sites is $N = L_x \times L_y$. We use finite DMRG with relatively large system sizes up to $N = 360$ to access more spin sectors and obtain the B dependence of the magnetization. Flux insertion simulations are carried out with infinite DMRG with a smaller unit cell of 144 sites, because flux insertion does not change the magnetization and the spin pumping is more robust with infinite DMRG algorithm. We mainly focus on the results on $L_y = 6$ cylinders and the results show almost no finite size effect in the x direction. We keep up to bond dimension $M = 6000$ to obtain accurate results with numerical truncation error $\epsilon \lesssim 1 \times 10^{-6}$; see more details in the SM [52].

III. PHASE DIAGRAM

The ground states of the J_1 - J_2 - J_χ model have been explored without the Zeeman effect, which results in CSLs with zero magnetization. Our numerical results are consistent with previous work in the range of parameters studied in Refs. [26, 27] with $h_z = 0$; see more details in SM [52].

By scanning over the parameter space of Eq. (2) we establish a global quantum phase diagram spanned by moiré lattice constants and magnetic fields [Fig. 1 (c)]. We identify three conventional magnetic phases including the 120° Néel phase, UUD phase, and stripe phase,

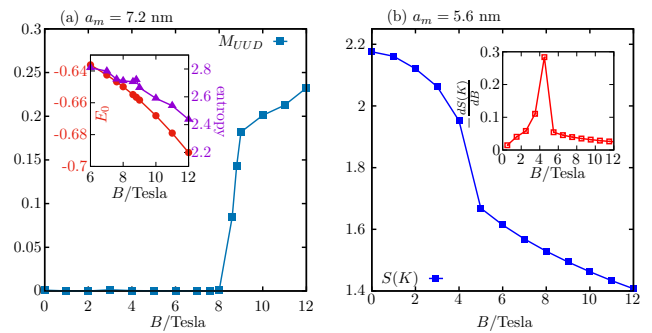


FIG. 3. (a) Order parameter of the UUD phase for various B at $a_m = 7.2$ nm with ground state energy per site E_0 and entanglement entropy in the inset. (b) Structure factor peak for various B at $a_m = 5.6$ nm. The results are obtained on $L_y = 6$ systems.

as well as a CSL phase. The rich quantum phase diagram results from frustrations and competing interactions, as the classical phase diagram only has Néel and UUD phases but no stripe phase. The stripe phase may originate purely from the quantum model, where the PP-CSL also exhibit stripelike polarizations; see more details of the classical Monte Carlo results in SM [52]. In the limit of $B = 0$ T the 120° Néel order dominates the whole range of a_m , where the nearest-neighbor J_1 takes the leading order, and it smoothly expands to nonzero B regimes. For a smaller value of $a_m < 5.6$ nm, the 120° Néel order becomes weak and the ground state might develop into a spin liquid on wider cylinders [56, 57] which is beyond the scope of the current work. At larger B , we find a stripe phase at small a_m and an UUD phase at larger a_m before the spins become fully polarized. Both phases exhibit a finite spin polarization in z -direction, which increases as B increases. In the intermediate B regime at small a_m , a CSL with partial polarization emerges. The topological nature of the CSL is identified as the $\nu = 1/2$ $SU(2)_1$ Laughlin state through the flux insertion simulations and the entanglement spectrum. The CSL extends to smaller a_m , but we are mainly interested in $a_m > 5.5$ nm, which corresponds to $\theta_m \lesssim 3.5^\circ$ where the moiré band fillings are fully tunable by the electrical gating [39]. The partially polarized stripe and UUD phases also extend beyond $B = 17$ T in our model. However, the energy scale of Zeeman interactions may interfere with other moiré bands, which goes beyond the scope of present work. This is especially true considering the larger g -factor for excitons [58].

IV. MAGNETIC ORDERS

The 120° Néel phase can be characterized by the static spin structure factor defined as $S(\mathbf{k}) = \frac{1}{N_m} \sum_{i,j} (\langle \mathbf{S}_i \cdot \mathbf{S}_j \rangle - \langle \mathbf{S}_i \rangle \langle \mathbf{S}_j \rangle) e^{i\mathbf{k} \cdot (\mathbf{r}_i - \mathbf{r}_j)}$, where we sum over $N_m = L_y \times L_y$ middle sites to minimize the boundary effects. $S(\mathbf{k})$ has prominent peaks at the \mathbf{K} points, suggesting the 120°

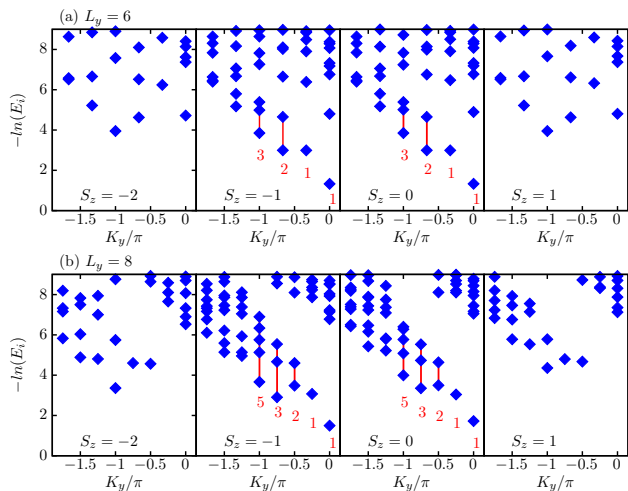


FIG. 4. Momentum resolved entanglement spectrum at $a_m = 5.6$ nm, $B = 15$ T in PP-CSL on (a) $L_y = 6$ and (b) $L_y = 8$. K_y is the conserved discrete momentum in the y direction. Quasi-degenerate eigenvalues are marked by $\{1, 1, 2, 3, \dots\}$ in each S_z sector.

spin correlations [Fig. 2 (a)]. Tuning finite B into the PP-CSL phase, the peaks disperse along the edge of the Brillouin zone with similar intensities and there is no distinctive peak [Fig. 2(b)]. By further increasing B into the stripe phase moderate peaks become concentrated at the \mathbf{M} points [Fig. 2(c)], indicating stripe correlations.

For larger a_m in the UUD phase there are mild peaks at the \mathbf{K} points [Fig. 2 (d)]. The magnitude of peaks decreases with increase of B which is consistent with a classical state. In order to determine the UUD order, where spins in the three-sublattice component form $\uparrow\uparrow\downarrow$, we define the order parameter as $M_{UUD} = \frac{1}{N} \sum_i | \langle S_i^z \rangle - \frac{1}{N} \sum_i \langle S_i^z \rangle |$ [59]. As shown in Fig. 3 (a), M_{UUD} increases suddenly around $B = 9$ T at $a_m = 7.2$ nm, indicating a first-order phase transition to the UUD phase. The inset of Fig. 3(a) shows the ground state energy as well as the entanglement entropy. The entanglement entropy exhibits a kink near the phase boundary which is consistent with the first-order phase transition. Meanwhile, we find smooth changes in energy and magnetization near the phase boundary; see SM [52]. The 120° Néel order and the UUD order share the same symmetry, therefore we cannot rule out the possibility of phase crossover.

Figure 3 (b) shows the structure factor peak at the \mathbf{K} points for various B . Fixing $a_m = 5.6$ nm, $S(\mathbf{K})$ has a sudden drop at $B = 5$ T, indicating the phase transition to CSL. Equivalently it could be seen from the peak in the first order derivative of $S(\mathbf{K})$ in the inset of Fig. 3(b). The phase transition could also be determined by the characteristic entanglement spectrum, which is discussed next.

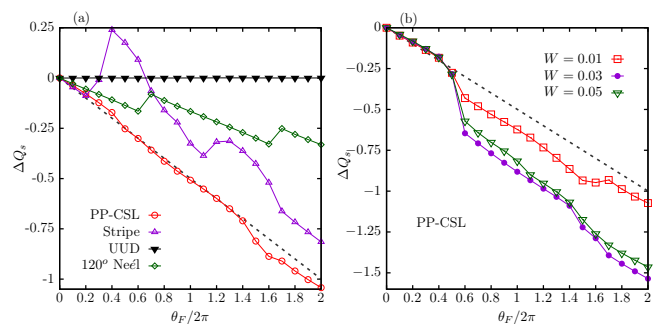


FIG. 5. (a) Flux insertion simulations in various phases on $L_y = 6$. For the PP-CSL phase, at 2π the spin pumping is almost $\frac{1}{2}$ fractionally quantized. After a 4π flux the total spin pumping is close to 1. (b) Flux insertion simulations with various disorder in the PP-CSL phase.

V. CHIRAL SPIN LIQUIDS

The entanglement spectrum extracted from the ground state provides an unbiased way to identify topological states through the one-to-one correspondence to the gapless edge excitation spectrum [60]. In the PP-CSL regime at $a_m = 5.6$ nm, $B = 15$ T, we find that the entanglement spectrum shows quasidegenerate patterns with decreasing momentum on both $L_y = 6$ and 8 , as shown in Figs. 4(a) and 4(b), respectively. The quasidegenerate eigenvalues form patterns of $\{1, 1, 2, 3, \dots\}$ in the lowest two S_z sectors, which agrees with the tower of states of the spinon sector [61, 62] by the $SU(2)_1$ Wess-Zumino-Witten theory of the $\nu = 1/2$ Laughlin state. Higher degenerate levels are not found because of the limited discrete momentum number in finite size lattices. For CSL, the spinon sector is found as the ground state in the presence of magnetic fields, where the vacuum sector has a higher energy.

Besides the entanglement spectrum, the spin flux insertion simulation can also identify the topological nature of the CSL [61, 63]. The spin flux θ_F is adiabatically inserted through the cylinder which adds a phase factor $S_i^+ S_j^- \rightarrow e^{i \frac{\theta_F}{L_y} (r_j^y - r_i^y)} S_i^+ S_j^-$ to the spin flip terms in the y direction. We measure the pumped spin using the reduced density matrix as $Q_s = \sum_\alpha \lambda_\alpha S_\alpha^z$ where λ_α is the eigenvalue and S_α^z is the corresponding S^z of the α eigenstate. Thus, the accumulated spin for different θ_F is $\Delta Q_s(\theta_F) = Q_s(\theta_F) - Q_s(0)$. As shown in Fig. 5 (a), the net spin pumping of $\Delta Q_s(\theta_F = 2\pi) \approx 0.5$ and $\Delta Q_s(\theta_F = 4\pi) \approx 1$ which corresponds to a spin Chern number $C = 0.5$ [61], suggesting again the Laughlin type CSL. This is similar to the $1/3$ fractional Chern insulator in the Haldane honeycomb lattice model [63]. Additionally, we find a disorder-averaged $\Delta Q_s(\theta_F = 4\pi) \approx 1$ in the presence of weak disorder $W = 0.01$ [Fig. 5 (b)] which is defined as $H_{\text{disorder}} = \sum_i w_i S_i^z$ with $|w_i| < W$ being a random effective onsite exchange field; see more details in SM [52]. At larger disorder $W > 0.03$, it deviates from

being quantized [64]. In the stripe and 120° Néel phases the spin pumping becomes not quantized [65] but finite due to a finite non-coplanar chiral order. Additionally, the spin pumping for the classical UUD phase is almost 0. Thus, phase boundaries between the PP-CSL and the stripe phase can be determined by the flux insertion as well as the entanglement spectrum.

Previous studies [27] have found a finite spin gap of the non-magnetic CSL without the Zeeman term. We also obtain the spin-1 gap as $\Delta_s = E_0(S_z^{total} = 1) - E_0(S_z^{total} = 0)$ in the non-magnetic CSL, which can be used to determine the spin response to the Zeeman field and partial polarization of the state in the thermodynamic limit. The spin gap in the bulk is almost the same for different L_x , showing little finite size effect. In the thermodynamic limit, if the Zeeman energy of flipping one spin is larger than the finite spin gap, the CSL is partially polarized. We find that the bulk spin gap is smaller in the whole CSL regime, thus the CSL always has partial spin polarization. For example, at $a_m = 5.6$ nm, $B = 15$ T a finite stripelike magnetization in the z direction appears with $\frac{1}{N} \sum_{x,y} (-1)^x S_{x,y}^z \approx 0.027$; see SM [52] for more details on the magnetization. The CSL with stripelike polarization and gapless spin excitation is distinctly different from the gapped non-magnetic CSL identified in the previous work [27]. Such a stripe has also been found on the honeycomb [66] and square lattice models [46] that coexist with CSL. However, in our results the stripelike spin polarization does not contribute to the transverse spin correlations, and the corresponding spin structure factor shows no distinctive peak in the PP-CSL.

VI. SUMMARY AND DISCUSSION

We have explored magnetic field induced phases in the TMD moiré heterobilayer $\text{WSe}_2/\text{MoSe}_2$ by studying a single-band Hubbard model that can be realized for twisted angles $\theta_m \lesssim 3.5$ [39]. Through extensive

DMRG simulations on quasi-one-dimensional cylinders, we map out the global quantum phase diagram spanned by twisted angles and magnetic fields. In particular, we have identified a CSL with partial spin polarization for intermediate magnetic fields, and showed its robust Chern number under weak disorder. Furthermore, the partially polarized CSL is surrounded by three magnetic phases including the 120° Néel phase, UUD phase, and stripe phase. The moiré superlattices with a tremendously large unit cell reduce the required B to generate strong enough chiral interactions for stabilizing the CSL. The transition from CSL to stripe phase with further increased B can be qualitatively compared to experiments of field induced magnetic transitions of spin-liquid-like phases [67]. For small to intermediate on-site Hubbard repulsion U the electron charge degrees of freedom cannot be neglected. Future studies may explore the field induced phases directly on the Hubbard model, where the CSL may be stabilized for an intermediate U even without B [23, 24]. Besides half filling, other commensurate fillings of moiré bands also provide a platform to explore CSL, where Wigner crystals are formed with charges localized in triangular and other types of superlattices [68–72]. Finally, we note that our study might also be relevant to a triangular-based spin- $\frac{1}{2}$ metal-organic framework, where the lattice constant can still be much larger than that of typical crystalline solids.

We thank Dr. Fengcheng Wu for helpful discussions. This work was carried out under the auspices of the U.S. Department of Energy (DOE) National Nuclear Security Administration (NNSA) under Contract No. 89233218CNA000001. It was supported by Center for Integrated Nanotechnologies (Y.H.), a DOE BES user facility, in partnership with the LANL Institutional Computing Program for computational resources, and Quantum Science Center (J.-X.Z.), a U.S. DOE Office of Science Quantum Information Science Research Center. D.N.S. was supported by U.S. DOE BES under Grant No. DE-FG02-06ER46305.

-
- [1] L. Balents, Spin liquids in frustrated magnets, *Nature* **464**, 199 (2010).
 - [2] L. Savary and L. Balents, Quantum spin liquids: a review, *Reports on Progress in Physics* **80**, 016502 (2016).
 - [3] Y. Zhou, K. Kanoda, and T.-K. Ng, Quantum spin liquid states, *Reviews of Modern Physics* **89**, 025003 (2017).
 - [4] C. Broholm, R. Cava, S. Kivelson, D. Nocera, M. Norman, and T. Senthil, Quantum spin liquids, *Science* **367**, 6475 (2020).
 - [5] V. Kalmeyer and R. B. Laughlin, Equivalence of the resonating-valence-bond and fractional quantum hall states, *Physical review letters* **59**, 2095 (1987).
 - [6] X.-G. Wen, Mean-field theory of spin-liquid states with finite energy gap and topological orders, *Physical Review B* **44**, 2664 (1991).
 - [7] X.-G. Wen, Quantum orders and symmetric spin liquids, *Physical Review B* **65**, 165113 (2002).
 - [8] T. Senthil and O. Motrunich, Microscopic models for fractionalized phases in strongly correlated systems, *Physical Review B* **66**, 205104 (2002).
 - [9] P. W. Anderson, The resonating valence bond state in La_2CuO_4 and superconductivity, *Science* **235**, 1196 (1987).
 - [10] R. Laughlin, The relationship between high-temperature superconductivity and the fractional quantum Hall effect, *Science* **242**, 525 (1988).
 - [11] P. A. Lee, N. Nagaosa, and X.-G. Wen, Doping a Mott insulator: Physics of high-temperature superconductivity, *Reviews of Modern Physics* **78**, 17 (2006).
 - [12] E. Fradkin, S. A. Kivelson, and J. M. Tranquada, Col-

- loquium: Theory of intertwined orders in high temperature superconductors, *Reviews of Modern Physics* **87**, 457 (2015).
- [13] A. Y. Kitaev, Fault-tolerant quantum computation by anyons, *Annals of Physics* **303**, 2 (2003).
- [14] C. Nayak, S. H. Simon, A. Stern, M. Freedman, and S. D. Sarma, Non-abelian anyons and topological quantum computation, *Reviews of Modern Physics* **80**, 1083 (2008).
- [15] T. Senthil, S. Sachdev, and M. Vojta, Fractionalized fermi liquids, *Physical Review Letters* **90**, 216403 (2003).
- [16] A. A. Patel, D. Chowdhury, A. Allais, and S. Sachdev, Confinement transition to density wave order in metallic doped spin liquids, *Physical Review B* **93**, 165139 (2016).
- [17] H.-C. Jiang, T. Devereaux, and S. Kivelson, Holon wigner crystal in a lightly doped kagome quantum spin liquid, *Physical Review Letters* **119**, 067002 (2017).
- [18] Y. Kasahara, T. Ohnishi, Y. Mizukami, O. Tanaka, S. Ma, K. Sugii, N. Kurita, H. Tanaka, J. Nasu, Y. Motome, *et al.*, Majorana quantization and half-integer thermal quantum hall effect in a kitaev spin liquid, *Nature* **559**, 227 (2018).
- [19] M. Ye, G. B. Halász, L. Savary, and L. Balents, Quantization of the thermal hall conductivity at small hall angles, *Physical review letters* **121**, 147201 (2018).
- [20] J. Bruin, R. Claus, Y. Matsumoto, N. Kurita, H. Tanaka, and H. Takagi, Robustness of the thermal hall effect close to half-quantization in α -RuCl₃, *Nature Physics* **18**, 401 (2022).
- [21] D.-H. Lee and M. P. A. Fisher, Anyon superconductivity and the fractional quantum Hall effect, *Phys. Rev. Lett.* **63**, 903 (1989).
- [22] F. Ming, X. Wu, C. Chen, K. D. Wang, P. Mai, T. A. Maier, J. Strockoz, J. W. F. Venderbos, C. González, J. Ortega, S. Johnston, and H. H. Weitering, Evidence for chiral superconductivity on a silicon surface, *Nature Physics* **19**, 500 (2023).
- [23] A. Szasz, J. Motruk, M. P. Zaletel, and J. E. Moore, Chiral spin liquid phase of the triangular lattice Hubbard model: a density matrix renormalization group study, *Physical Review X* **10**, 021042 (2020).
- [24] B.-B. Chen, Z. Chen, S.-S. Gong, D. Sheng, W. Li, and A. Weichselbaum, Quantum spin liquid with emergent chiral order in the triangular-lattice hubbard model, *Physical Review B* **106**, 094420 (2022).
- [25] S.-S. Gong, W. Zheng, M. Lee, Y.-M. Lu, and D. Sheng, Chiral spin liquid with spinon fermi surfaces in the spin- $\frac{1}{2}$ triangular Heisenberg model, *Physical Review B* **100**, 241111 (2019).
- [26] A. Wietek and A. M. Läuchli, Chiral spin liquid and quantum criticality in extended $s=\frac{1}{2}$ Heisenberg models on the triangular lattice, *Physical Review B* **95**, 035141 (2017).
- [27] S.-S. Gong, W. Zhu, J.-X. Zhu, D. N. Sheng, and K. Yang, Global phase diagram and quantum spin liquids in a spin- $\frac{1}{2}$ triangular antiferromagnet, *Physical Review B* **96**, 075116 (2017).
- [28] Y.-H. Zhang, D. Sheng, and A. Vishwanath, SU(4) chiral spin liquid, exciton supersolid, and electric detection in moiré bilayers, *Physical Review Letters* **127**, 247701 (2021).
- [29] C. Kuhlenkamp, W. Kadow, A. Imamoglu, and M. Knap, Tunable topological order of pseudo spins in semiconductor heterostructures, arXiv preprint arXiv:2209.05506 (2022).
- [30] T. Cookmeyer, J. Motruk, and J. E. Moore, Four-spin terms and the origin of the chiral spin liquid in Mott insulators on the triangular lattice, *Physical Review Letters* **127**, 087201 (2021).
- [31] Y. Shimizu, K. Miyagawa, K. Kanoda, M. Maesato, and G. Saito, Spin liquid state in an organic Mott insulator with a triangular lattice, *Physical Review Letters* **91**, 107001 (2003).
- [32] Y. Kurosaki, Y. Shimizu, K. Miyagawa, K. Kanoda, and G. Saito, Mott transition from a spin liquid to a fermi liquid in the spin-frustrated organic conductor κ -(ET)₂Cu₂(CN)₃, *Phys. Rev. Lett.* **95**, 177001 (2005).
- [33] S. Yamashita, Y. Nakazawa, M. Oguni, Y. Oshima, H. Nojiri, Y. Shimizu, K. Miyagawa, and K. Kanoda, Thermodynamic properties of a spin-1/2 spin-liquid state in a κ -type organic salt, *Nature Physics* **4**, 459 (2008).
- [34] T. Itou, A. Oyamada, S. Maegawa, M. Tamura, and R. Kato, Quantum spin liquid in the spin-1/2 triangular antiferromagnet EtMe₃Sb[Pd(dmit)₂]₂, *Physical Review B* **77**, 104413 (2008).
- [35] M. Yamashita, N. Nakata, Y. Kasahara, T. Sasaki, N. Yoneyama, N. Kobayashi, S. Fujimoto, T. Shibauchi, and Y. Matsuda, Thermal-transport measurements in a quantum spin-liquid state of the frustrated triangular magnet κ -(BEDT-TTF)₂Cu₂(CN)₃, *Nature Physics* **5**, 44 (2009).
- [36] T. Itou, A. Oyamada, S. Maegawa, and R. Kato, Instability of a quantum spin liquid in an organic triangular-lattice antiferromagnet, *Nature Physics* **6**, 673 (2010).
- [37] H. Zhou, E. Choi, G. Li, L. Balicas, C. Wiebe, Y. Qiu, J. Copley, and J. S. Gardner, Spin liquid state in the S=1/2 triangular lattice Ba₃CuSb₂O₉, *Physical Review Letters* **106**, 147204 (2011).
- [38] M. M. Bordelon, E. Kenney, C. Liu, T. Hogan, L. Posthuma, M. Kavand, Y. Lyu, M. Sherwin, N. P. Butch, C. Brown, *et al.*, Field-tunable quantum disordered ground state in the triangular-lattice antiferromagnet NaYbO₂, *Nature Physics* **15**, 1058 (2019).
- [39] F. Wu, T. Lovorn, E. Tutuc, and A. H. MacDonald, Hubbard model physics in transition metal dichalcogenide moiré bands, *Physical review letters* **121**, 026402 (2018).
- [40] Y. Tang, L. Li, T. Li, Y. Xu, S. Liu, K. Barmak, K. Watanabe, T. Taniguchi, A. H. MacDonald, J. Shan, and K. F. Mak, Simulation of Hubbard model physics in WSe₂/WS₂ moiré superlattices, *Nature* **579**, 353 (2020).
- [41] F. Wu, T. Lovorn, E. Tutuc, I. Martin, and A. MacDonald, Topological insulators in twisted transition metal dichalcogenide homobilayers, *Physical Review Letters* **122**, 086402 (2019).
- [42] L. Wang, E.-M. Shih, A. Ghiotto, L. Xian, D. A. Rhodes, C. Tan, M. Claassen, D. M. Kennes, Y. Bai, B. Kim, *et al.*, Correlated electronic phases in twisted bilayer transition metal dichalcogenides, *Nature Materials* **19**, 861 (2020).
- [43] T. Li, S. Jiang, B. Shen, Y. Zhang, L. Li, Z. Tao, T. Devakul, K. Watanabe, T. Taniguchi, L. Fu, *et al.*, Quantum anomalous hall effect from intertwined moiré bands, *Nature* **600**, 641 (2021).
- [44] R. Haghshenas, S.-S. Gong, and D. Sheng, Single-layer tensor network study of the Heisenberg model with chiral interactions on a kagome lattice, *Physical Review B* **99**, 174423 (2019).
- [45] C. Hickey, L. Cincio, Z. Papić, and A. Paramekanti,

- Haldane-Hubbard Mott insulator: From tetrahedral spin crystal to chiral spin liquid, *Physical Review Letters* **116**, 137202 (2016).
- [46] Y. Huang, W. Zhu, S.-S. Gong, H.-C. Jiang, and D. N. Sheng, Coexistence of non-abelian chiral spin liquid and magnetic order in a spin-1 antiferromagnet, *Physical Review B* **105**, 155104 (2022).
- [47] C. Hickey, L. Cincio, Z. Papić, and A. Paramekanti, Emergence of chiral spin liquids via quantum melting of noncoplanar magnetic orders, *Physical Review B* **96**, 115115 (2017).
- [48] S. R. White, Density matrix formulation for quantum renormalization groups, *Physical Review Letters* **69**, 2863 (1992).
- [49] S. R. White, Density-matrix algorithms for quantum renormalization groups, *Physical Review B* **48**, 10345 (1993).
- [50] K. Kumar, H. J. Changlani, B. K. Clark, and E. Fradkin, Numerical evidence for a chiral spin liquid in the XXZ antiferromagnetic heisenberg model on the kagome lattice at $m=2/3$ magnetization, *Physical Review B* **94**, 134410 (2016).
- [51] A. H. MacDonald, S. Girvin, and D. t. Yoshioka, t expansion for the hubbard model, *Physical Review B* **37**, 9753 (1988).
- [52] See Supplemental Material at [URL will be inserted by publisher] for more detailed numerical results.
- [53] U. Schollwöck, The density-matrix renormalization group in the age of matrix product states, *Annals of physics* **326**, 96 (2011).
- [54] M. Fishman, S. R. White, and E. M. Stoudenmire, The ITensor Software Library for Tensor Network Calculations, *SciPost Phys. Codebases*, 4 (2022).
- [55] J. Hauschild and F. Pollmann, Efficient numerical simulations with Tensor Networks: Tensor Network Python (TeNPy), *SciPost Phys. Lect. Notes*, 5 (2018), code available from <https://github.com/tenpy/tenpy>, arXiv:1805.00055.
- [56] W.-J. Hu, S.-S. Gong, W. Zhu, and D. Sheng, Competing spin-liquid states in the spin-1 2 heisenberg model on the triangular lattice, *Physical Review B* **92**, 140403 (2015).
- [57] Z. Zhu and S. R. White, Spin liquid phase of the $S=1/2$ J_1 - J_2 heisenberg model on the triangular lattice, *Physical Review B* **92**, 041105 (2015).
- [58] J. Förste, N. V. Tepliakov, S. Y. Kruchinin, J. Lindlau, V. Funk, M. Förg, K. Watanabe, T. Taniguchi, A. S. Baimuratov, and A. Högele, Exciton g-factors in monolayer and bilayer WSe_2 from experiment and theory, *Nature Communications* **11**, 4539 (2020).
- [59] Y. Li, S. Bachus, H. Deng, W. Schmidt, H. Thoma, V. Hutanu, Y. Tokiwa, A. A. Tsirlin, and P. Gegenwart, Partial up-up-down order with the continuously distributed order parameter in the triangular antiferromagnet $TmMgGaO_4$, *Physical Review X* **10**, 011007 (2020).
- [60] H. Li and F. D. M. Haldane, Entanglement spectrum as a generalization of entanglement entropy: Identification of topological order in non-abelian fractional quantum hall effect states, *Physical review letters* **101**, 010504 (2008).
- [61] S.-S. Gong, W. Zhu, and D. Sheng, Emergent chiral spin liquid: Fractional quantum Hall effect in a kagome heisenberg model, *Scientific Reports* **4**, 6317 (2014).
- [62] Y.-C. He, D. Sheng, and Y. Chen, Obtaining topological degenerate ground states by the density matrix renormalization group, *Physical Review B* **89**, 075110 (2014).
- [63] A. G. Grushin, J. Motruk, M. P. Zaletel, and F. Pollmann, Characterization and stability of a fermionic $\nu=1/3$ fractional chern insulator, *Physical Review B* **91**, 035136 (2015).
- [64] W. Zhu and D. Sheng, Disorder-driven transition in the $\nu=5/2$ fractional quantum Hall effect, *Physical Review Letters* **123**, 056804 (2019).
- [65] Y. Huang and D. Sheng, Topological chiral and nematic superconductivity by doping mott insulators on triangular lattice, *Physical Review X* **12**, 031009 (2022).
- [66] T. A. Sedrakyan, L. I. Glazman, and A. Kamenev, Spontaneous formation of a nonuniform chiral spin liquid in a moat-band lattice, *Physical Review Letters* **114**, 037203 (2015).
- [67] J. Xing, L. D. Sanjeeva, J. Kim, G. Stewart, A. Podlesnyak, and A. S. Sefat, Field-induced magnetic transition and spin fluctuations in the quantum spin-liquid candidate $CsYbSe_2$, *Physical Review B* **100**, 220407 (2019).
- [68] E. C. Regan, D. Wang, C. Jin, M. I. Bakti Utama, B. Gao, X. Wei, S. Zhao, W. Zhao, Z. Zhang, K. Yumigeta, *et al.*, Mott and generalized Wigner crystal states in WSe_2/WSe_2 moiré superlattices, *Nature* **579**, 359 (2020).
- [69] X. Huang, T. Wang, S. Miao, C. Wang, Z. Li, Z. Lian, T. Taniguchi, K. Watanabe, S. Okamoto, D. Xiao, *et al.*, Correlated insulating states at fractional fillings of the WSe_2/WSe_2 moiré lattice, *Nature Physics* **17**, 715 (2021).
- [70] J. Motruk, D. Rossi, D. A. Abanin, and L. Rademaker, Kagome chiral spin liquid in transition metal dichalcogenide moiré bilayers, *Physical Review Research* **5**, L022049 (2023).
- [71] J. Cai, E. Anderson, C. Wang, X. Zhang, X. Liu, W. Holtzmann, Y. Zhang, F. Fan, T. Taniguchi, K. Watanabe, *et al.*, Signatures of fractional quantum anomalous hall states in twisted $MoTe_2$, *Nature* **622**, 63 (2023).
- [72] Interaction-driven topological phase diagram of twisted bilayer $MoTe_2$, .

Supplemental Material for “Magnetic field induced partially polarized chiral spin liquid in a transition metal dichalcogenide moiré system”

In the Supplemental Material, we provide more numerical results to support the conclusions we have discussed in the main text. In Sec. I, we provide examples of the finite bond dimension scaling of the ground state energy as well as entanglement entropy in the partially polarized-chiral spin liquid (PP-CSL) phase and show the numerical convergence of Density Matrix Renormalization Group (DMRG) results. We also show the details of the disorder averaged spin pumping in the presence of a weak disorder. In Sec. II, we show the magnetization of different phases in real space. In Sec. III, we show various spin interactions as a function of the moiré lattice constant a_m and magnetic field B . In Sec. IV, we show the phase diagram without considering the Zeeman interactions and compare it with our main results. In Sec. V, we implement the classical Monte Carlo methods and obtain the classical phase diagram of the model to compare with our main results. In Sec. VI, we show the magnetization evolution with increasing B from the 120° Néel phase to Up-up-down (UUD) phase. In Sec. VII, we show the evolution of the chiral order for various B from the 120° Néel phase to PP-CSL phase.

I. DMRG CONVERGENCE

The convergence of DMRG calculation can be examined by the finite bond dimension (M) extrapolation of the ground state energy. We show the obtained ground-state energy per site E_0 versus the inverse DMRG bond dimension ($1/M$) for $L_y = 6$ from both finite DMRG and infinite DMRG results. For finite DMRG, in order to minimize the boundary effect, we extract the energy using the middle $3/4$ (which is $L_x/8 < x \leq 7L_x/8$) of the lattices and calculate the entanglement entropy using the left and right subsystems divided at $L_x/2$. We keep the bond dimensions up to $M = 6000$. In Fig. S1 (a) and (b), we show the energies E_0^{Mid} and entanglement entropy at $a_m = 5.6$ nm, $B = 15$ T on $L_y = 6$ with finite and infinite DMRG results, as an example in the PP-CSL phase. The E_0^{Mid} and entropy are extrapolated by the second-order polynomials $C(1/M) = C(0) + a/M + b/M^2$, where $C(0)$ is the extrapolated result in the infinite M limit. The energies converge smoothly with bond dimension and the extrapolated energies are very close to the lowest energies we obtain, indicating the good convergence of the results.

The spin flux insertion results in the PP-CSL show slight difference for different M . As shown in Fig. S2(a), the spin pumping at smaller $M = 1200$ have large variations due to a finite magnetization and the pumping is less than 1 at $\theta_F = 4\pi$. As M increases, the pumping becomes more uniform and the pumped spin is closer to the quantized value of 1.

In the presence of a disorder, we perform an average over random disorder configurations to obtain the averaged spin pumping. The results in the main text are calculated with $M = 3000$ and up to 30 disorder configuration averages. To examine the numerical convergence we show the disorder averaged spin pumping $\Delta Q_s(\theta_F)$ for various number of random disorder configurations $N_{\text{configuration}}$ at $W = 0.01$ in Fig. S3. For $M = 2500$ in Fig. S3(a) the $\Delta Q_s(\theta_F = 2\pi)$ remains almost the same for $N_{\text{configuration}} = 10$ to 50, indicating the converged results for disorder average. Similarly for $M = 3000$ in Fig. S3(b) the disorder averaged $\Delta Q_s(\theta_F)$ is converged with $N_{\text{configuration}}$ up to 30. During the simulations for $W = 0.01$, we find that although for a small number of disorder configurations the spin pumping has a sudden drop and becomes much larger than 1, most of the $\Delta Q_s(\theta_F = 2\pi)$ at given random disorder configurations is close to 1. Comparing the results of $M = 2500, 3000, 3500$ in Fig. S2(b) we find that using larger bond dimensions can reduce the sudden drop of $\Delta Q_s(\theta_F)$ and lead to the averaged spin pumping of closer to 1. On the other hand, for $W > 0.03$ most of the $\Delta Q_s(\theta_F = 2\pi)$ at given random disorder configurations are much larger than 1, which shows distinct difference from the $W = 0.01$ results.

II. MAGNETIZATION IN REAL SPACE FOR DIFFERENT PHASES

We show the magnetization in real space with infinite DMRG for the stripe phase, the PP-CSL phase, the UUD phase, and the 120° Néel phase in Fig. S4 (a), (b), (c), and (d), respectively. In the stripe phase there are small spin polarization in z -direction which is stripe-like as shown in Fig. S4(a), consistent with the stripe spin-spin correlations given in the main text. In the PP-CSL phase [Fig. S4(b)] the stripe-like spin polarization becomes much weaker, and shows a positive spin polarization on every site. We also notice that the stripe changes direction in the PP-CSL phase. In the UUD phase the z -component of the spin dominates and the spins in the three-sublattice component form $\uparrow\uparrow\downarrow$, which indicates a classical spin alignment, as shown in Fig. S4(c). For the 120° Néel phase at small but finite B we also find a very small spin polarization as shown in Fig. S4(d). The phase is consistent with the 120° Néel order at $B = 0$ T where the spin-spin correlations are mainly in the xy plane.

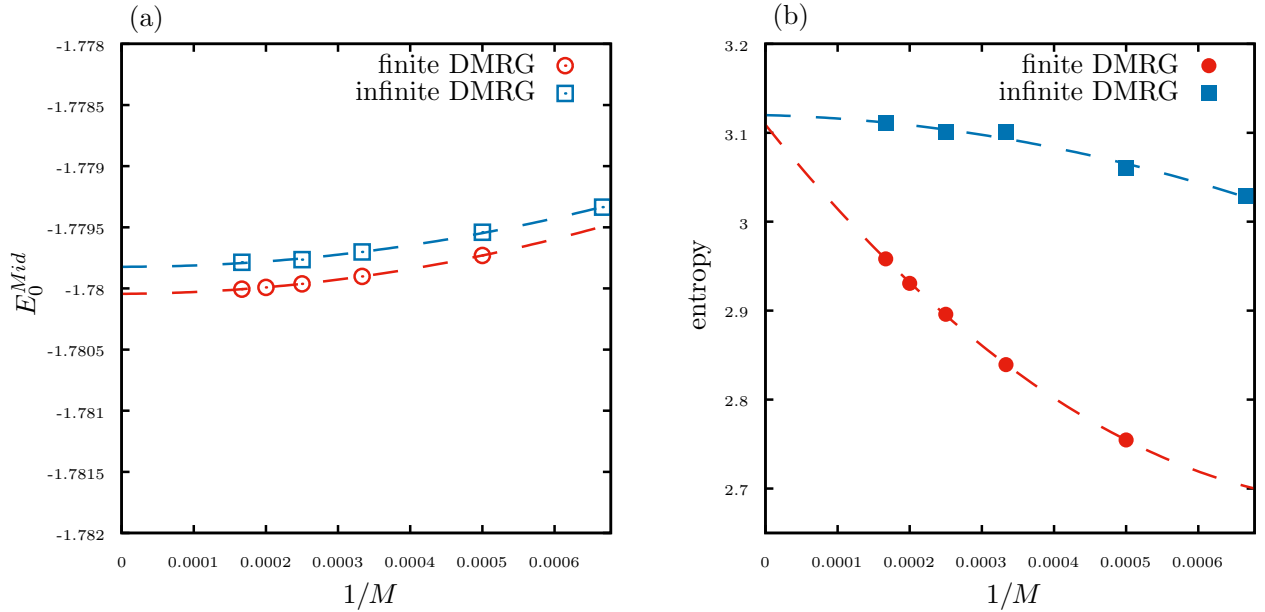


FIG. S1. Finite bond dimension scaling of the (a) ground state energy per site E_0^{Mid} and (b) entanglement entropy in the PP-CSL phase on a $L_y = 6$ cylinder. The $L_x = 48$ for finite DMRG results.

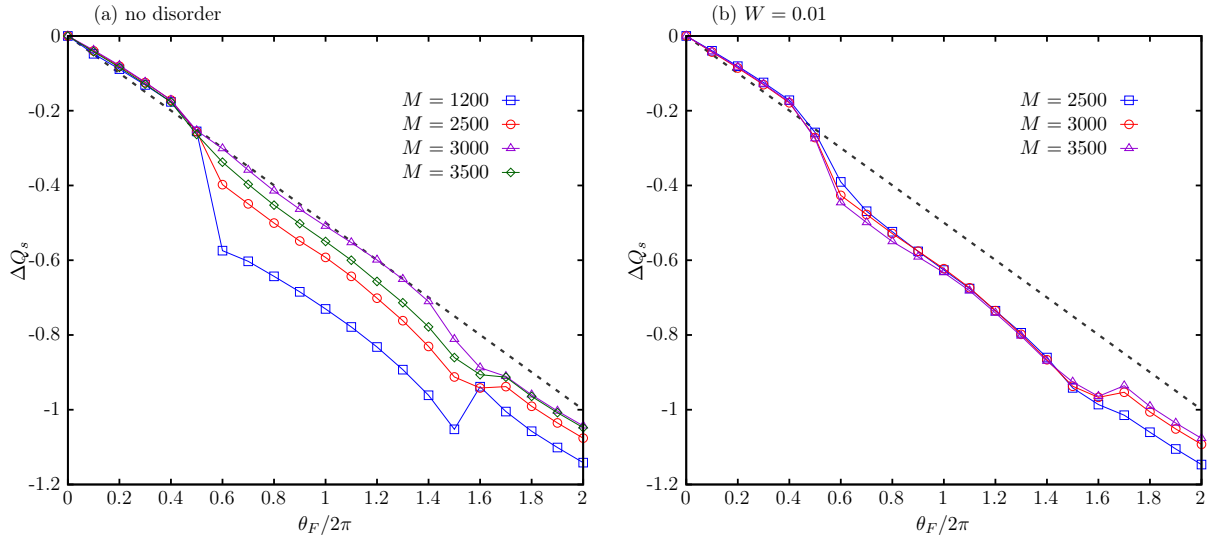


FIG. S2. The spin flux insertion using various bond dimensions M in the PP-CSL phase at $a_m = 5.6$ nm, $B = 15$ T on a $L_y = 6$ cylinder with (a) $W = 0$ (no disorder) and (b) $W = 0.01$.

III. a_m AND B DEPENDENCE OF SPIN INTERACTION PARAMETERS

To relate to previous works on the triangular J_1 - J_2 - J_χ spin-1/2 model we show parameters as a function of a_m and B . The coupling parameters in the effective spin model are $J_1 = 4t_1^2/U - 28t_1^4/U^3$, $J_2 = 4t_2^2/U + 4t_1^4/U^3$, $J_\chi = 24t_1^3 \sin(e\Phi_B/\hbar)/U^2$, where $\Phi_B = 2\pi B \frac{\sqrt{3}}{4} a_m^2$ is the magnetic flux through each unit triangle, and $2h_z = \mu_B g_s B$ where μ_B is the Bohr magneton and the spin g-factor $g_s \approx 2$. The a_m and B dependence of t_1 , t_2 and U are obtained from Ref. [39].

Fixing the same $B = 10$ T, Fig. S5 (a) shows the J_2/J_1 , Fig. S5 (b) shows the J_χ/J_1 , and Fig. S5 (c) shows the $2h_z/J_1$ for various a_m . J_2/J_1 does not depend on B , which decreases as a_m increases. J_χ/J_1 does not have much

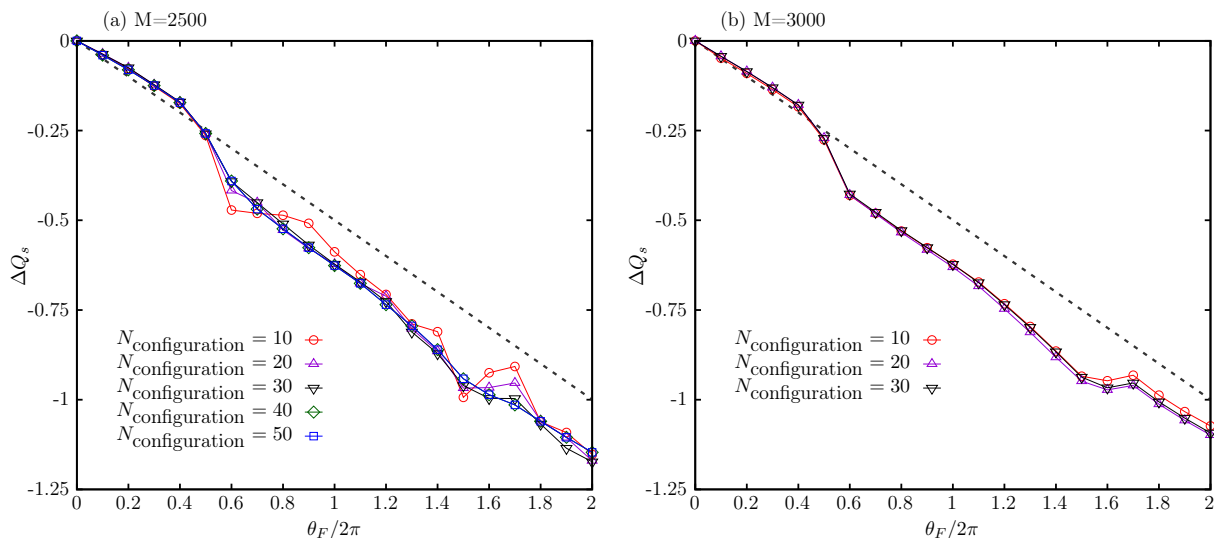


FIG. S3. The disorder averaged spin flux insertion using various number of random disorder configurations with $W = 0.01$ in the PP-CSL phase at $a_m = 5.6$ nm, $B = 15$ T on a $L_y = 6$ cylinder obtained with (a) $M = 2500$ and (b) $M = 3000$.

dependence on a_m , mainly because as a_m increases the magnetic flux increases but the interaction strength decreases at the same time. Since the strength $2h_z$ does not depend on a_m while J_1 decreases as a_m increases, the Zeeman term becomes more dominant at large a_m .

We also show the parameter dependence with fixing $a_m = 5.6$ nm. Figure S6 shows the same spin interaction parameters as Fig. S5, where J_χ/J_1 and $2h_z/J_1$ increases as B increases, while J_2/J_1 remains the same.

IV. PHASE DIAGRAM WITHOUT ZEEMAN INTERACTIONS

To connect with previous numerical studies of the chiral spin liquids on the triangle lattice with finite chiral interactions, we obtain the phase diagram without considering the Zeeman term ($h_z = 0$) based on the $L_y = 6$ system. The resulting J_1 - J_2 - J_χ model has spin $SU(2)$ symmetry and $\sum_i S_i^z = 0$ in the ground state with no spin polarization. As shown in Fig. S7, the 120° Néel phase is stabilized at small B , and CSL at large B . For even larger B , a tetrahedral order is expected as the chiral interactions become dominant, leading to a magnetically ordered state [26, 27]. Notice that the CSL phase has a larger regime compared to the phase diagram with the Zeeman term, we believe that the spin Zeeman effect of the magnetic field favors the magnetically ordered state while the orbital effect of the magnetic field promotes the CSLs.

V. CLASSICAL PHASE DIAGRAM

To highlight the important quantum fluctuation and correlation effect, we obtain the classical phase diagram of the same model using the classical Monte Carlo methods on the $L_y \times L_x = 12 \times 12$ system with periodic boundary conditions on both x and y directions. We use the simulated annealing with exponentially decaying temperatures down to $0.01 meV/k_B$ to approximate the ground state. At each temperature we perform 8×10^5 sweeps utilizing the SpinMC package.

As shown in Fig. S8, the classical phase diagram only has the 120° Néel phase stabilized at small B , and the Up-up-down phase at large B . The chiral spin liquid is a quantum spin liquid that has no classic analog. In addition, the stripe order can only be stabilized considering full quantum fluctuations because the CSL also emerges with the stripe like magnetization. The classical 120° Néel phase contains all spins in one plane, which can be rotated freely with the same energy. Using the spin structure factor we find prominent peaks at the \mathbf{K} points suggesting the 120° spin correlations, as shown in Fig. S9. We further characterize the classical 120° Néel phase by the spin-spin correlations $\mathbf{S}_i \cdot \mathbf{S}_j = |S_i||S_j|\cos(\theta_{ij})$ between neighboring bonds as shown in Fig. S10 (a). All bonds have negative correlations of around -0.5 , which corresponds to $\theta_{ij} \approx 120^\circ$.

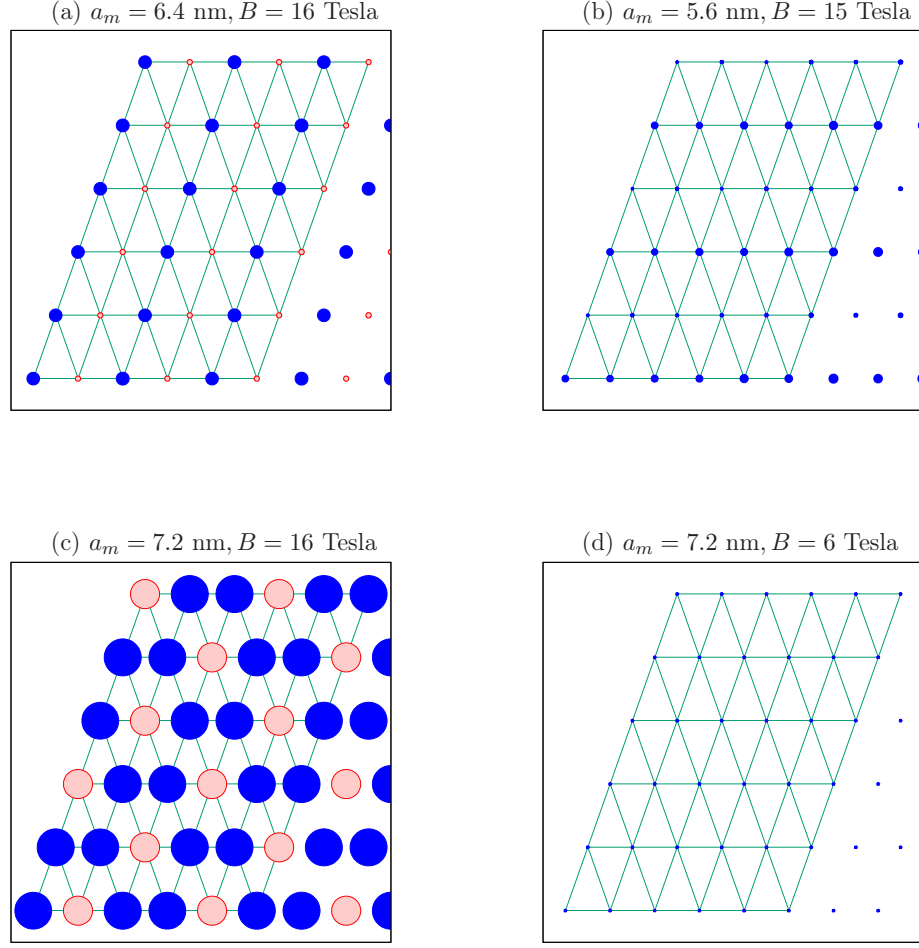


FIG. S4. Magnetization for (a) the stripe phase, (b) the PP-CSL phase, (c) the UUD phase, and (d) the 120° Néel phase. The blue solid circles represent positive spin values, and the red shaded circles represent negative spin values. The radius represents the magnitude where the blue ones in (a), (c), (d) have $\langle S_i^z \rangle \approx 0.14, 0.41, 0.03$, respectively. The larger blue circles in (b) has $\langle S_i^z \rangle \approx 0.01$ where the radius is amplified by 10 to see the circle clearer.

On the other hand, the classical Up-up-down phase at large B has a different pattern of spin correlations as shown in Fig. S10 (b). The correlations along the hexagon are positive indicating the “Up” spin, and the correlations between them and the hexagonal center are negative, indicating the “Down” spin at the center. Interestingly, we find that the two “Up” spins in the classical UUD phase has an angle around $\theta_{ij} \approx 30^\circ$. The UUD phase can be further confirmed by the $\langle S_i^z \rangle$ value (the magnetic field is also along z direction) as shown in Fig. S11, where the spins in the three-sublattice component form $\uparrow\uparrow\downarrow$.

To characterize the phase transition between the 120° Néel phase and the Up-up-down phase, we obtain the energy per site E_0 and its first order derivative as a function of B . As shown in Fig. S12 (a), at $a_m = 7.2$ nm, E_0 has a sudden drop at $B = 13.5$, where its first order derivative shows minimum value, indicating a phase transition [see Fig. S12 (b)]. Even though the chiral interactions cannot induce chiral spin liquid in the classical phase diagram, it also plays an important role. Because without the chiral interactions dE_0/dB decreases almost linearly over the increase of B , which is as expected due to the Zeeman term.

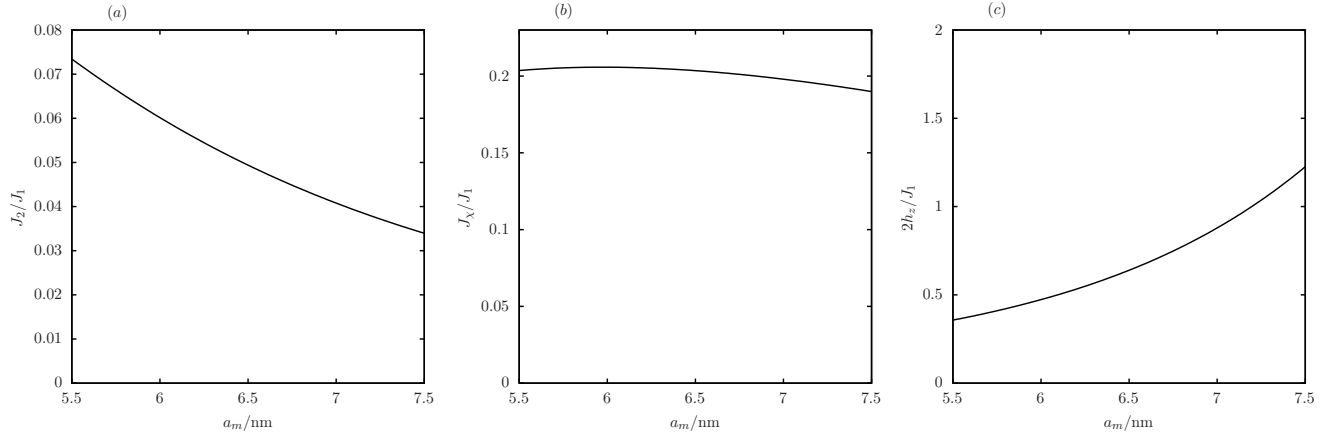


FIG. S5. Various spin interaction parameters at $B = 10$ T for various a_m . (a) shows the J_2/J_1 , (b) shows the J_X/J_1 , and (c) shows the $2h_z/J_1$.

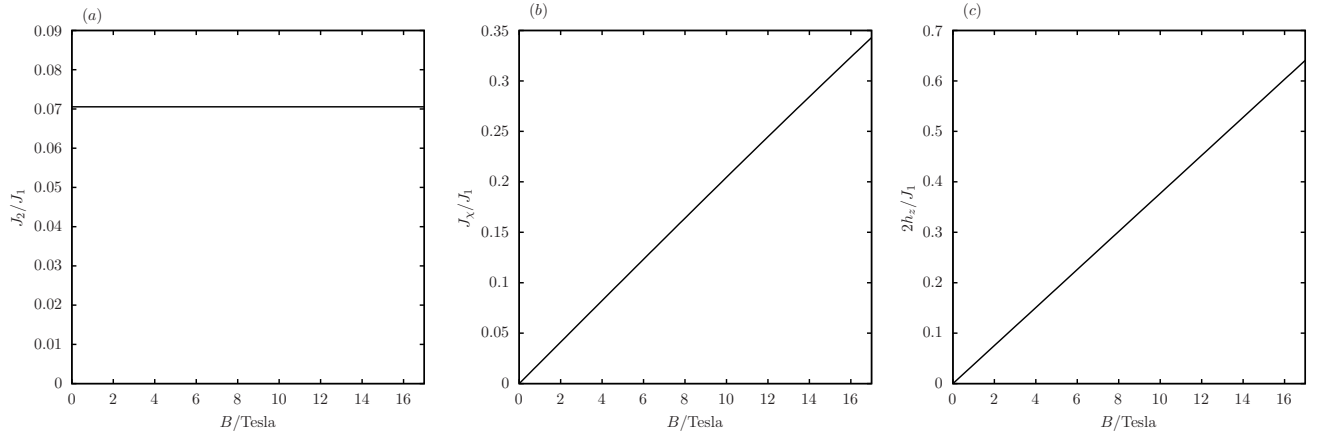


FIG. S6. Various spin interaction parameters at $a_m = 5.6$ T for various B . (a) shows the J_2/J_1 , (b) shows the J_X/J_1 , and (c) shows the $2h_z/J_1$.

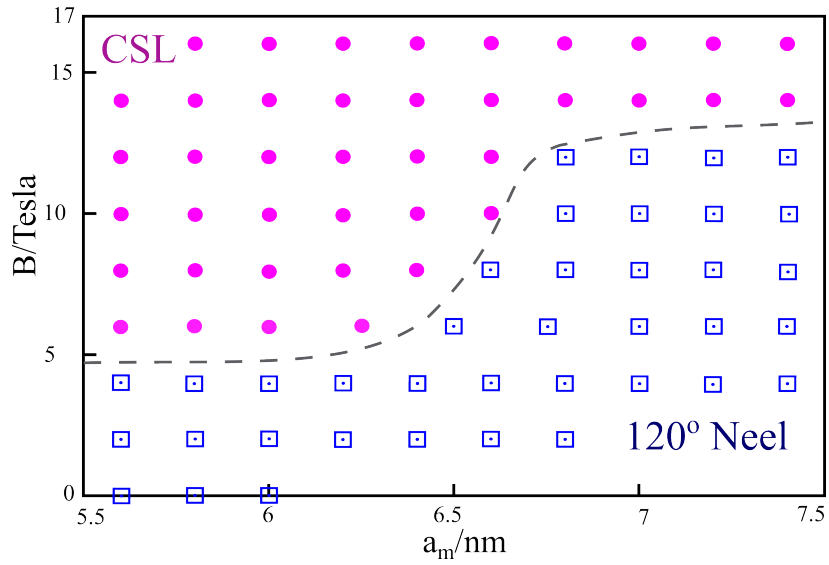


FIG. S7. The phase diagram without the Zeeman term.

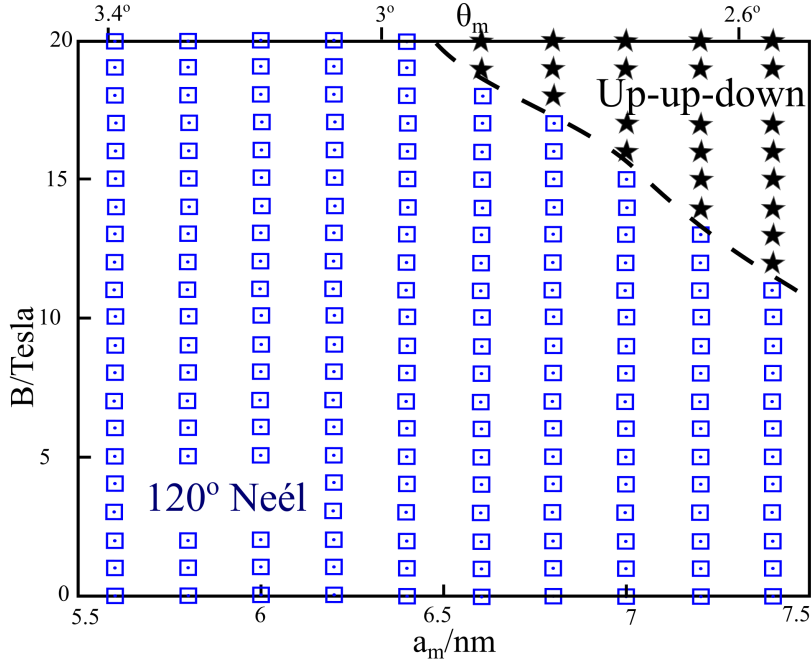


FIG. S8. The classical phase diagram obtained by the classical Monte Carlo methods. 120° Néel phase is identified for small B at all a_m , and the Up-up-down phase is identified at large B and a_m similar to the quantum phase diagram. The chiral spin liquid and stripe phase are not identified in the classical phase diagram.

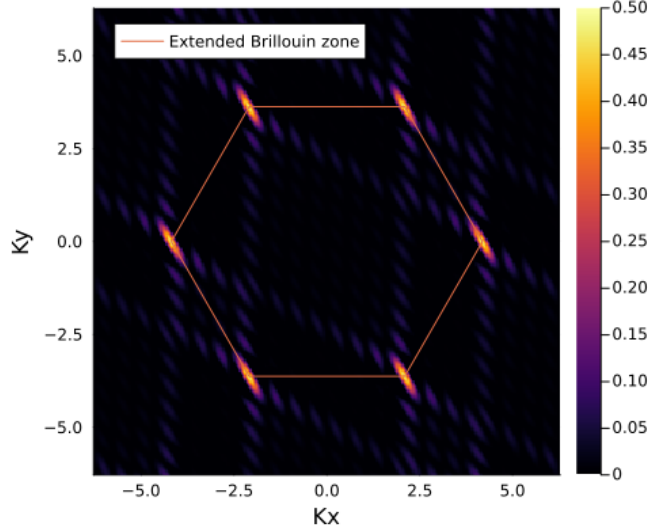


FIG. S9. The spin structure factor from classical Monte Carlo methods, obtained with $a_m = 7.2$ nm, $B = 0$ T. The red lines indicate the extended Brillouin zone where the peaks are at K points.

VI. MAGNETIZATION FROM THE 120° NÉEL PHASE TO THE UUD PHASE

The magnetization is obtained by using the middle half of the lattice to minimize the boundary effect. In order to access more total spin sectors, we use the $N = 60 \times 6$ lattice with finite DMRG methods. As shown in Fig. S13, the magnetization is 0 in the limit of $B = 0$ T and it smoothly increases as B increases from the 120° Néel phase to the UUD phase.

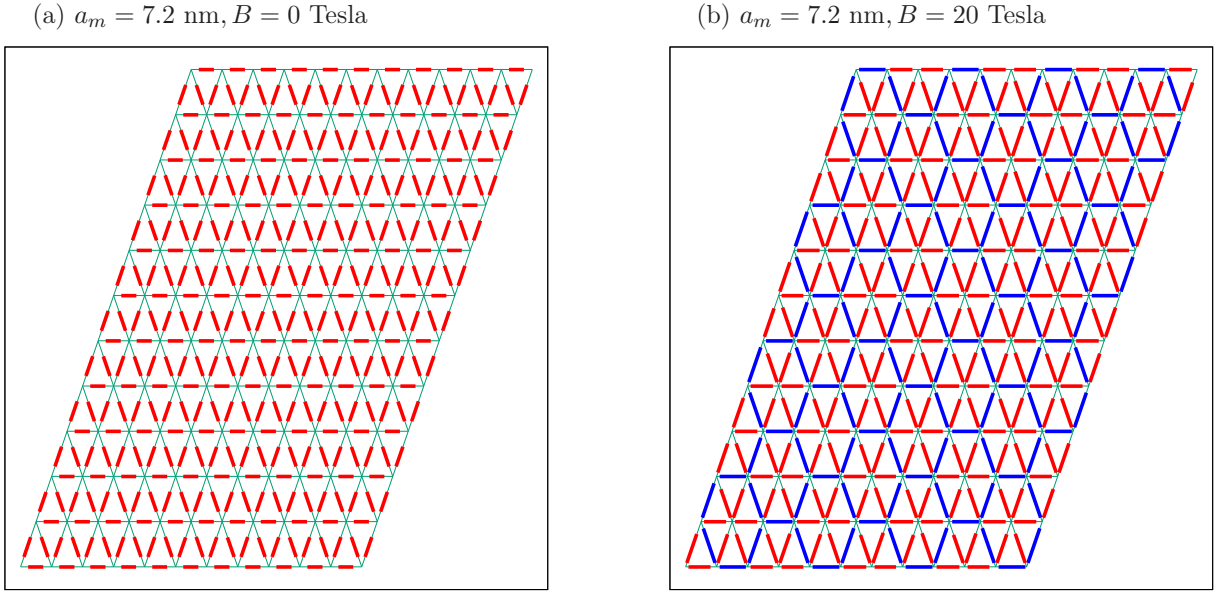


FIG. S10. The spin-spin correlations between neighboring sites from classical Monte Carlo methods. The 12×12 lattice is drawn with green color. The blue color represent positive spin-spin correlations and the red color represent negative spin-spin correlations between neighboring sites. The length represents the magnitude where the red ones in (a) are around 0.5. The blue ones in (b) are around 0.88.

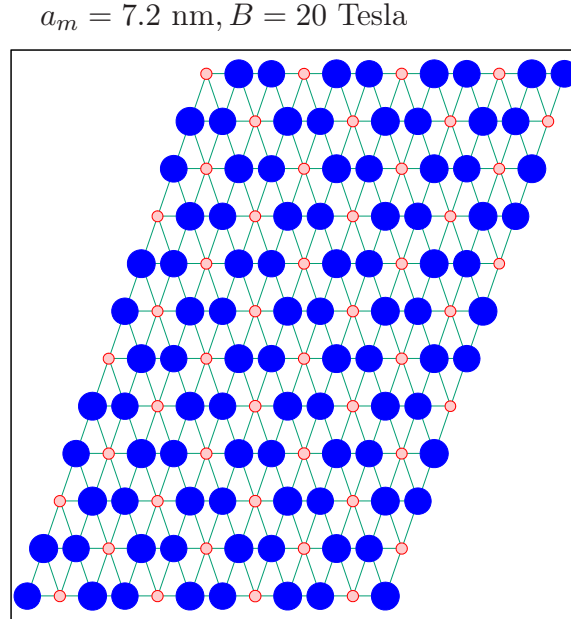


FIG. S11. The $\langle S_i^z \rangle$ from classical Monte Carlo methods, obtained with $a_m = 7.2 \text{ nm}, B = 20 \text{ T}$. The blue solid circles represent positive spin values, and the red shaded circles represent negative spin values. The radius represents the magnitude where the blue ones are about 0.4.

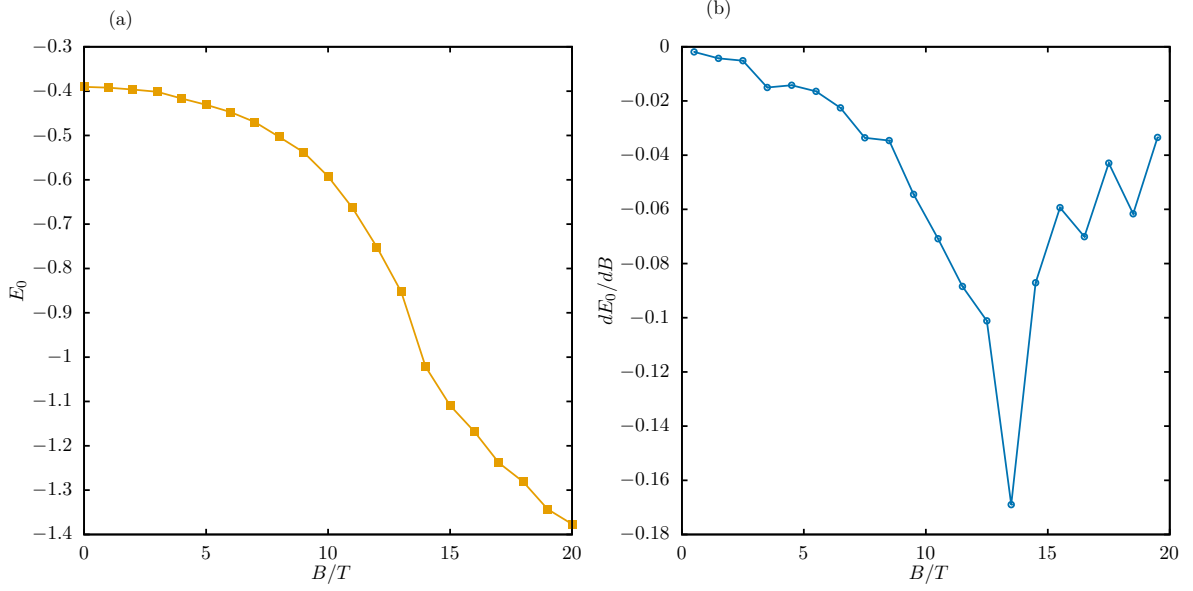


FIG. S12. (a) The energy per site (E_0) and (b) the derivative of the energy with respect to B from classical Monte Carlo methods, obtained with $a_m = 7.2$ nm.

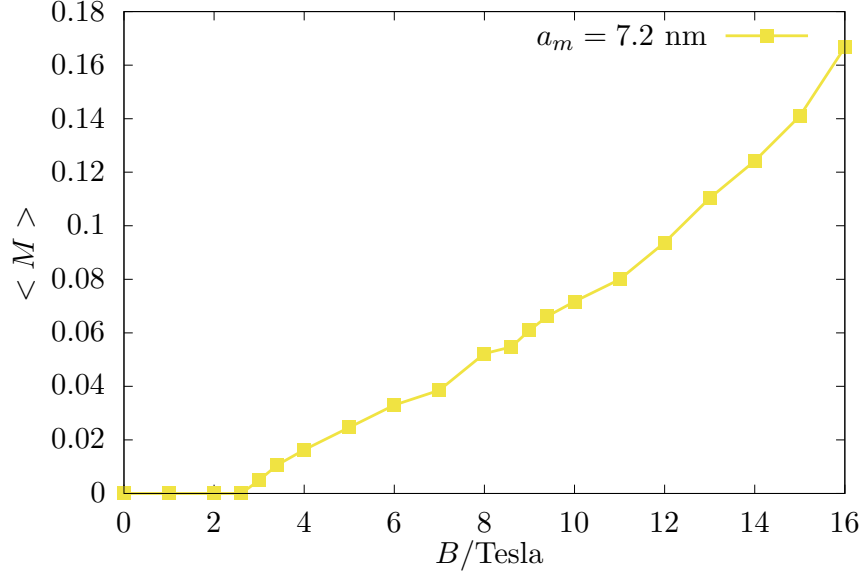


FIG. S13. The magnetization $\langle M \rangle$ at $a_m = 7.2$ nm for various B .

VII. CHIRAL ORDER FROM THE 120° NÉEL PHASE TO THE CSL PHASE

The chiral order is studied on a finite $N = 48 \times 6$ lattice, which is defined as $\langle \chi \rangle = 1/(N-1) \sum_{\{ijk\} \in \Delta/\nabla} \mathbf{S}_i \cdot (\mathbf{S}_j \times \mathbf{S}_k)$ due to the open boundary. As shown in Fig. S14, the chiral order smoothly increases as B increases from the 120° Néel phase to the CSL phase and it does not show a critical behavior near the phase transition point of around $B = 5$ T. We believe larger systems may be needed to see the critical behavior. The phase boundary between the 120° Néel phase and the CSL phase is determined by the characteristic counting in the entanglement spectrum.

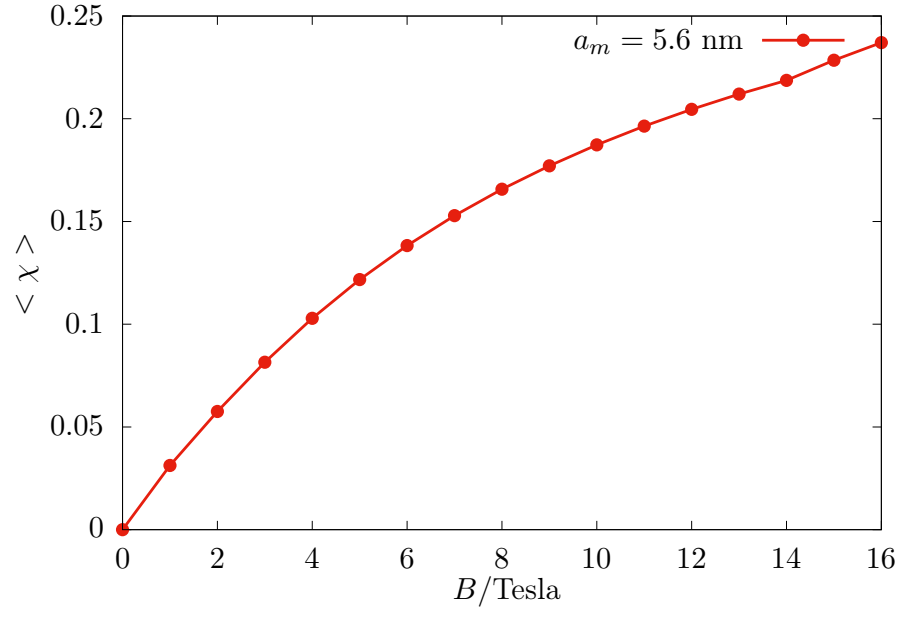


FIG. S14. The chiral order $\langle \chi \rangle$ at $a_m = 5.6 \text{ nm}$ for various B .